

# SCIENTIFIC REPORTS

OPEN

## Understanding stability diagram of perpendicular magnetic tunnel junctions

Witold Skowroński<sup>1</sup>, Maciej Czapkiewicz<sup>1</sup>, Sławomir Ziętek<sup>1</sup>, Jakub Chęciński<sup>1,2</sup>, Marek Frankowski<sup>1</sup>, Piotr Rzeszut<sup>1</sup> & Jerzy Wrona<sup>3</sup>

Perpendicular magnetic tunnel junctions (MTJ) with a bottom pinned reference layer and a composite free layer (FL) are investigated. Different thicknesses of the FL were tested to obtain an optimal balance between tunneling magnetoresistance (TMR) ratio and perpendicular magnetic anisotropy. After annealing at 400 °C, the TMR ratio for 1.5 nm thick CoFeB sublayer reached 180% at room temperature and 280% at 20 K with an MgO tunnel barrier thickness corresponding to the resistance area product  $RA = 10 \text{ Ohm } \mu\text{m}^2$ . The voltage vs. magnetic field stability diagrams measured in pillar-shaped MTJs with 130 nm diameter indicate the competition between spin transfer torque (STT), voltage controlled magnetic anisotropy (VCMA) and temperature effects in the switching process. An extended stability phase diagram model that takes into account all three effects and the effective damping measured independently using broadband ferromagnetic resonance technique enabled the determination of both STT and VCMA coefficients that are responsible for the FL magnetization switching.

Magnetic tunnel junctions (MTJs) have become a basic building block for various types of spintronics devices, such as magnetic random access memory (MRAM) cells, magnetic field sensors and microwave generators or detectors<sup>1</sup>. The properties of spintronics devices, such as thermal stability of an MRAM cell<sup>2</sup> or sensitivity of microwave detectors<sup>3</sup> utilizing MTJs can be greatly improved by using magnetic layers with perpendicular anisotropy<sup>4</sup>. Among a few ways to realize such a perpendicular MTJ, taking advantage of the interface anisotropy component<sup>5</sup> yields the best results so far, especially in terms of high tunneling magnetoresistance (TMR) ratio, which is measured typically in MTJs with CoFeB/MgO/CoFeB trilayer. Recent studies on perpendicular MTJ showed the TMR ratio exceeding 200%<sup>6</sup> thanks to careful optimization of both the free layer (FL) and reference layer (RL) structure<sup>7</sup>. In addition, one of the key challenges for the commercial development of spin transfer torque (STT)-MRAM is to optimize perpendicular MTJ to withstand the temperature budget introduced at the back end of line CMOS fabrication process with temperatures up to 400 °C. To achieve this a precise design of the layer stack, taking into account all constituent layers as well as the properties and the treatment of the bottom electrode, has to be performed.

In this letter, we report on the perpendicular MTJ with a composite CoFeB/W/CoFeB FL<sup>8,9</sup> which is characterized by high perpendicular magnetic anisotropy and spin polarization resulting in up to 180% TMR measured at room temperature and above 280% TMR at low temperature. The RL is pinned to a synthetic ferromagnet (SyF) consisting of Co/Pt super-lattices<sup>10</sup> coupled by a thin Ru spacer. Electrical transport measurements were performed in MTJs patterned into 130-nm diameter pillar. Voltage vs. perpendicular magnetic field switching diagrams<sup>11,12</sup> are measured in order to separate between STT, voltage control of magnetic anisotropy (VCMA) and temperature effects. An analytic model based on work by Bernert *et al.*<sup>13</sup> was extended to reproduce the experimental results.

### Results

**Wafer-level characterization.** The multilayers with the following structure were deposited: bottom electrode/Ta seed/[Co (0.5)/Pt (0.2)] × 6/Co (0.6)/Ru (0.8)/Co (0.6)/[Pt (0.2)/Co (0.5)] × 3/W (0.25)/CoFeB (1.0)/MgO (0.8)/CoFeB ( $t_{\text{FL}}$ )/W (0.2)/CoFeB (0.5)/MgO (0.75)/Ta (3.0)/top electrode (thicknesses in nm), with  $t_{\text{FL}}$

<sup>1</sup>AGH University of Science and Technology, Department of Electronics, Al. Mickiewicza 30, 30-059, Kraków, Poland.

<sup>2</sup>AGH University of Science and Technology, Faculty of Physics and Applied Computer Science, Al. Mickiewicza 30, 30-059, Kraków, Poland. <sup>3</sup>Singulus Technologies AG, Hanauer Landstrasse 103, Kahl am Main, 63796, Germany.

Correspondence and requests for materials should be addressed to W.S. (email: [skowron@agh.edu.pl](mailto:skowron@agh.edu.pl))

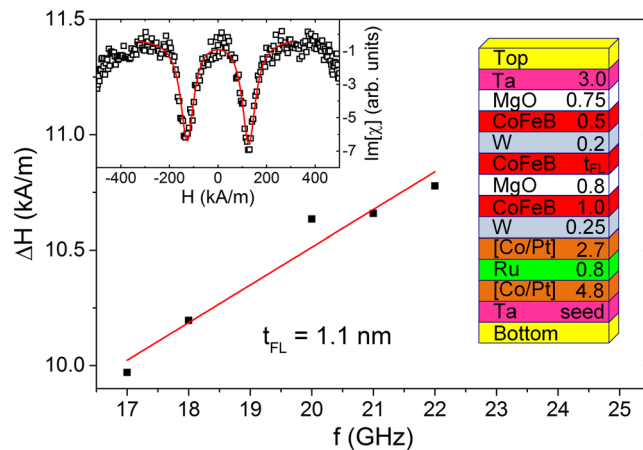


**Figure 1.** FMR linewidth (full symbols) as a function of the excitation frequency for MTJ with  $t_{FL} = 1.1$  nm together with a fit (solid line) to the Eq. (2). Inset presents the measured imaginary part of the magnetic susceptibility (open symbols) as a function of the magnetic field for  $f = 19$  GHz together with a fit to the Eq. (6) (solid line). Toy picture presents a schematic of the investigated multilayer structure.

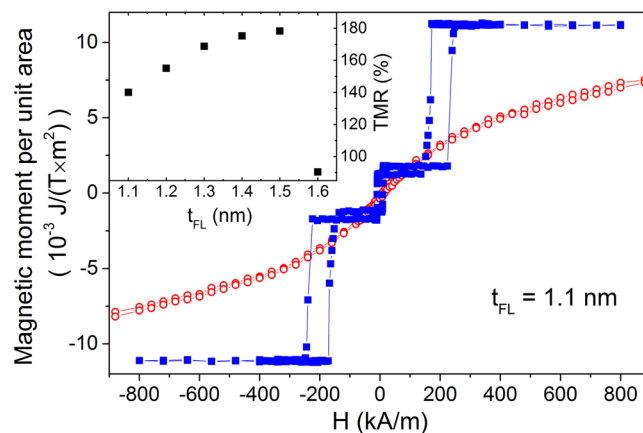


**Figure 2.** Magnetic moment per unit area vs. in-plane (open symbols) and perpendicular (full symbols) magnetic field of the MTJ with  $t_{FL} = 1.1$  nm. Inset presents the TMR ratio dependence on  $t_{FL}$  measured using CIPT method.

ranging from 1.1 up to 1.6 nm. The schematics of the multilayer stack is presented in Fig. 1. The bottom Co/Pt super-lattices coupled by a thin Ru spacer are characterized by high perpendicular magnetic anisotropy (PMA). The W-based separator between the superlattices and the reference layer ensures high ferromagnetic coupling between the top super-lattice and the RL. In addition, it provides structural transition from a face center cubic  $SyF^{14}$  to a body center cubic CoFeB and contributes to the absorption of B atoms from CoFeB during annealing and crystallization processes. Damping parameter was measured using ferromagnetic resonance (FMR) (see Methods section). Figure 1 presents the dependence of the  $\Delta H$  on the excitation frequency.

Vibrating sample magnetometry (VSM) measurements of a representative sample with  $t_{FL} = 1.1$  nm presented in Fig. 2 reveal independent switching of the FL (at small magnetic fields below 50 kA/m) and RL (at high magnetic fields between 150 and 300 kA/m), which ensures bistable parallel (P) and antiparallel (AP) state. The FL magnetization was calculated and yielded  $\mu_0 M_S = 1.12$  T. An inset of Fig. 2 depicts the TMR ratio for different  $t_{FL}$  measured on the wafer-level using current in-plane tunneling (CIPT) method. An increase of the TMR from 140% for  $t_{FL} = 1.1$  nm up to TMR = 180% for  $t_{FL} = 1.5$  nm is explained by an increase of the spin polarization for the thicker ferromagnetic layer. A rapid reduction of the TMR for  $t_{FL} = 1.6$  nm is caused by the transition of the FL magnetization vector to the sample plane. After the patterning process the TMR ratio measured in the nano-pillar was about 5–15% lower comparing to the result obtained from CIPT method, which can be explained by the appearance of the small serial parasitic resistance. This small resistance, however, has negligible influence on the MTJ parameters derived afterwards.

Figure 3 presents the TMR vs. magnetic field dependence measured in the MTJ nanopatterned into pillars of 130-nm in diameter with different  $t_{FL}$ . Increase in  $t_{FL}$  leads to an increase in TMR ratio and decrease in the

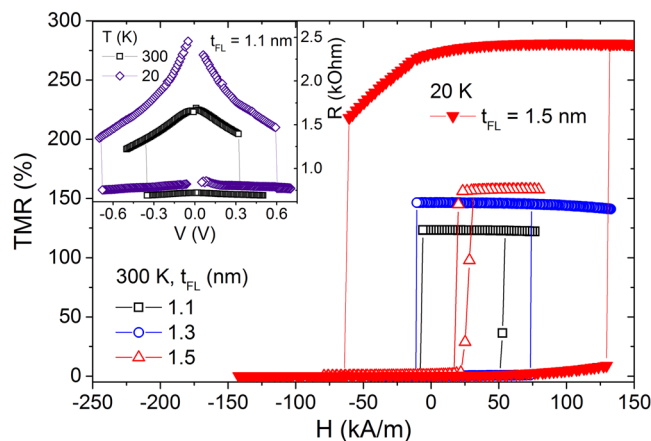


**Figure 3.** TMR vs. magnetic field loop of MTJs with different  $t_{FL}$  measured at room temperature (300 K). Significantly smaller coercive field  $H_C$  is measured for  $t_{FL} = 1.5$  nm, which increases at  $T = 20$  K. An inset presents a resistance vs. voltage switching loop measured in an external magnetic field of  $H = 25$  kA/m, obtained at  $T = 300$  K (squares) and  $T = 20$  K (circles).

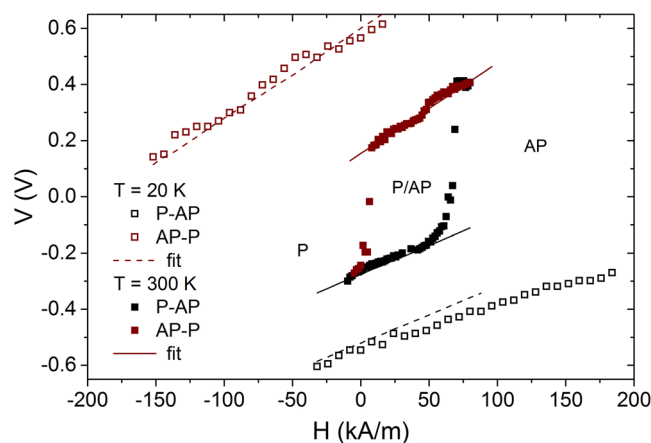


**Figure 4.** Voltage vs. magnetic field stability diagram measured in the MTJ with  $t_{FL} = 1.1$  nm at  $T = 20$  K (open symbols) and  $T = 300$  K (full symbols). Dotted lines represents approximation based on Eq. (4). An extended model based on correction presented in Eq. (5) is represented by dashed (20 K) and solid (300 K) lines.

coercive field. The offset field of about  $H_S = 25$  kA/m originates from the stray field, which depends on the MTJ lateral size (not shown here).

**Stability diagram.** To further elucidate the properties of the fabricated MTJ, current (voltage)-induced switching loops were measured in the presence of the perpendicular magnetic field. An inset of Fig. 3 presents a representative resistance vs. voltage loop measured in a magnetic field compensating the offset field in the MTJ with  $t_{FL} = 1.1$  nm. It has been already established that apart from the conventional STT effect observed in MTJs with relatively thin MgO barriers, the switching process can be also affected by the VCMA effect in devices with a thin FL<sup>15,16</sup>. To investigate the switching process in more detail, we repeated the  $R(V)$  loop measurements, with different constant magnetic field. The stability diagram obtained in this way both at room temperature ( $T = 300$  K) and low temperature ( $T = 20$  K) for the MTJ with  $t_{FL} = 1.1$  nm is presented in Fig. 4. To understand these diagrams, the following fitting procedure was used. First, low-temperature data were modeled using Eq. (4) to obtain switching field  $H_W$ ,  $H_S$  (being the offset field measured at low bias voltage) and STT coefficients, which are little affected by heat. The slope of  $V(H)$  depends mostly on damping-like torque  $-a_{DL}$  (see modelling details in Methods section), whereas the vertical offset is adjusted by  $H_W$  – solid lines in Fig. 4. Next, to compensate the offset between AP-P and P-AP switching voltages, (which take place at opposite electric field applied to the MgO/CoFeB interface) VCMA coefficient  $k_V$  was introduced according to the Eq. (5), without temperature influence so far ( $k_t = 0$ ). Finally, thermal reduction of  $H_W$  was introduced by adjusting  $k_t$  to fit the stability diagram obtained at room temperature. Independently, we simulated the Joule-heating effect in our MTJ pillar and we found negligible temperature increase, therefore, we assumed constant temperature in our analysis.

$t_{\text{FL}}$ (nm)	$H_C$ (kA/m)	$\kappa$ (fJ/Vm)	$\tau_{\text{DL}}$ (Nm)	$\alpha$ (no units)	$M_{\text{eff}}$ (kA/m)
1.1	264	46	$4.5 \times 10^{-19}$	0.038	-450
1.3	280	73	$4.5 \times 10^{-19}$	0.044	-150
1.5	72	66	$5.9 \times 10^{-19}$	0.087	-0.5

**Table 1.** Summary of the obtained perpendicular MTJ parameters.

In addition, for the precise derivation of the STT coefficients, the magnetization damping was calculated based on an independent FMR measurement presented in Methods section and included in Table 1.

## Discussion

Fitting the experimental stability diagram to the Eqs (4) and (5) yielded the temperature coefficients of  $k_i = 0.0014$  1/K. This parameter was kept constant for MTJs with different  $t_{\text{FL}}$ . Remaining parameters of the stability diagrams for each  $t_{\text{FL}}$  were modeled independently. For  $t_{\text{FL}} = 1.1$  nm, the following STT components were obtained  $a_{\text{DL}} = 0.024$  T/V and  $a_{\text{FL}} = 0.02$  T/V<sup>2</sup>, however, we note that the modeled stability diagram is only little sensitive to  $a_{\text{FL}}$ , which agrees with another macrospin approach based on LLG equation presented in Ref. 17. Damping-like torque  $\tau_{\text{DL}}$  was thereafter recalculated using Eq. (1):

$$\tau_{\text{DL}} = \frac{M_S v \tau_{\text{LLG}}}{\gamma} \quad (1)$$

where  $v$  is the FL volume and  $\tau_{\text{LLG}} = -(\gamma a_{\text{DL}})$ , where  $\gamma$  is the gyromagnetic ratio (see details in Methods section). As the result we obtained  $\tau_{\text{DL}} = 4.5 \times 10^{-19}$  Nm/V, which agrees well with literature values of STT in case of an in-plane MTJ<sup>18–20</sup>. Regarding the VCMA, the best results for MTJ with  $t_{\text{FL}} = 1.1$  nm were obtained for  $k_V = 0.12$  1/V. Based on the following relation:  $k_V = \kappa / \mu_0 H_C M_S t_{\text{FL}} t_B$ , where  $t_B = 0.82$  nm is the tunnel barrier thickness, VCMA coefficient of  $\kappa = 46$  fJ/Vm was calculated, which fits well the commonly measured values for CoFeB/MgO devices<sup>21,22</sup> VCMA and STT coefficients of all investigated MTJs are gathered in Table 1.

The damping-like torque component obtained from the stability diagram is almost constant as a function of  $t_{\text{FL}}$ , which is explained by little dependence of the TMR ratio, and thus the spin polarization, on the ferromagnetic layer thickness in the investigated regime. The VCMA coefficient is comparable for MTJs with  $t_{\text{FL}} = 1.3$  nm and 1.5 nm and greater than in MTJ with  $t_{\text{FL}} = 1.1$  nm. This behavior is expected, as for thicker  $t_{\text{FL}}$  the absolute value of the effective magnetization is reduced and it is more susceptible to the anisotropy change induced by the electric field<sup>23</sup>. Moreover, in the same thickness regime, where the transition between perpendicular and in-plane anisotropy occurs, the effective damping increases, which may be attributed to an increase in the level of magnetization disorder<sup>24</sup>.

In conclusion, we investigated perpendicular MTJs with composite CoFeB/W/CoFeB FL of different thickness and SyF Co/Pt/Ru-pinned RL. In the investigated FL thickness range we observed an increase of the effective damping extracted from the broadband FMR measurements with increasing FL thickness, which is mainly caused by the reduction of the effective anisotropy. After patterning MTJs into nano-meter scale pillars, we measured the resistance vs. voltage loops for different external magnetic field amplitudes and created the stability diagrams for each FL thickness. To model the experimental data, we included the thermal and VCMA terms into the theoretical STT-switching phase diagram. Based on the fitting procedure, we obtained STT components together with the VCMA coefficient. Our findings shine more light on the switching process of MTJs applied in future MRAM technologies.

## Methods

**Sample deposition and nano-fabrication.** Multilayer samples were deposited using Singulus TIMARIS sputtering system on chemically-mechanically polished 4-inch Si wafers. After the deposition, the samples were annealed at 400 °C to induce proper crystallographic orientation of Fe-rich CoFeB and PMA of the CoFeB/MgO interfaces. Wafer-level parameters of the deposited multilayers were investigated by CIPT<sup>25</sup>, VSM and broadband FMR methods<sup>26</sup>. The latter was performed by measuring the complex transmission coefficient ( $S_{21}$ ) in a dedicated coplanar waveguide with a  $10 \times 8$  mm unpatterned sample placed face down. The frequency of the vector network analyzer is kept between 4 and 22 GHz, while sweeping the perpendicular magnetic field in  $\pm 550$  kA/m range.

Selected MTJs were patterned into circular cross-section pillars with diameter ranging from 130 up to 980 nm by means of electron-beam lithography, ion-beam etching and lift-off process.

The transport properties presented in this work were measured for the smallest devices with the area of  $A = 0.013 \mu\text{m}^2$  in a dedicated probe station equipped with magnetic field source. Four-probe method with a voltage source was used to apply 1-ms long pulses and measure the resistance during this voltage-pulse application. The stability diagrams were determined by sweeping the voltage pulses amplitude in the presence of a given magnetic field. Selected devices were characterized at low temperatures of  $T = 20$  K in order to determine the temperature influence on the magnetization switching properties.

**Modelling.** Magnetization damping was calculated based on linewidth  $\Delta H$ , which was measured using FMR technique and fitted by the Eq. (2):

$$\Delta H = \frac{4\pi\alpha f}{\gamma_0} + \Delta H_0 \quad (2)$$

Magnetization direction of the FL ( $\vec{m}_{\text{FL}}$ ) was calculated based on the Landau-Lifschitz-Gilbert (LLG) equation with the following STT components taken into account:

$$\begin{aligned} \frac{d\vec{m}_{\text{FL}}}{dt} = & -\gamma_0 \vec{m}_{\text{FL}} \times \vec{H}_{\text{eff}} + \alpha \vec{m}_{\text{FL}} \times \frac{d\vec{m}_{\text{FL}}}{dt} \\ & -\gamma_0 a_{\text{DL}} \frac{VR_{\text{p}}}{R} (\vec{m}_{\text{FL}} \times (\vec{m}_{\text{FL}} \times \vec{m}_{\text{RL}})) \\ & -\gamma_0 a_{\text{FL}} \left( \frac{VR_{\text{p}}}{R} \right)^2 (\vec{m}_{\text{FL}} \times \vec{m}_{\text{RL}}) \end{aligned} \quad (3)$$

where  $\gamma_0 = \gamma \mu_0$ , with the gyromagnetic ratio  $\gamma = (g \mu_{\text{B}}) / \hbar = 28 \text{ GHz/T}$ ,  $\mu_0$  is the permeability of the free space,  $g$  is the Lande spectroscopic splitting factor,  $\mu_{\text{B}}$  is the Bohr magneton,  $\hbar$  is the reduced Planck's constant,  $a_{\text{DL}}$  and  $a_{\text{FL}}$  are the damping-like and field-like STT coefficients expressed in T/V and T/V<sup>2</sup> units, respectively,  $\alpha$  is the magnetization damping,  $R$  and  $R_{\text{p}}$  are the MTJ resistance in a given state and minimal (parallel state) resistance,  $H_{\text{eff}}$  is the effective magnetic field:  $H_{\text{eff}} = H \pm H_{\text{W}} + H_{\text{S}}$ , where,  $H$  is the external perpendicular field,  $H_{\text{W}}$  is the switching field and  $H_{\text{S}}$  is the offset field.

Stability diagram was modeled based on ref. 13:

$$V_{\text{C}} = \frac{a_{\text{DL}} R}{2\alpha a_{\text{FL}} R_{\text{p}}} - \sqrt{\left( \frac{a_{\text{DL}} R}{2\alpha a_{\text{FL}} R_{\text{p}}} \right)^2 - \frac{\mu_0 R^2}{a_{\text{FL}} R_{\text{p}}^2} H_{\text{eff}}^2} \quad (4)$$

where,  $V_{\text{C}}$  is the switching voltage. It was assumed that damping-like (field-like) torque component is a linear (quadratic) function of the applied current<sup>20</sup>. To account for the additional physical effects that contribute to the stability diagram, namely VCMA and temperature,  $H_{\text{W}}$  is scaled by the factor:

$$H_{\text{W}} = H_{\text{C}} (1 - k_{\text{V}} V - \sqrt{k_{\text{T}} T}) \quad (5)$$

where  $V$  is the applied voltage,  $H_{\text{C}}$  is the coercive field,  $k_{\text{V}}$  is the VCMA coefficient<sup>27, 28</sup> and  $T$  is the ambient temperature. The dependence of the switching field on the temperature is represented by  $k_{\text{T}}$ , which in the first approximation is a square-root function<sup>29</sup>.

We note that for the discussed device size, the switching process may not be entirely uniform, however in Ref. 30 the authors found substantial deviations from the macrospin evolution only for MTJs of diameter greater than 150 nm.

The damping factor was measured independently by the broadband FMR technique. For each microwave frequency  $f$ , the complex magnetic susceptibility vs. magnetic field  $\chi(H)$  is extracted from  $S_{21}$  measurement by subtracting the magnetic independent offset and time-dependent drift<sup>31</sup>:

$$\chi(H) = \frac{M_{\text{eff}}(H - M_{\text{eff}})}{(H - M_{\text{eff}})^2 - H_{\text{f}}^2 - i \frac{\Delta H}{2} (H - M_{\text{eff}})} \quad (6)$$

where  $M_{\text{eff}} = M_{\text{S}} - H_{\text{K}}$  is the effective magnetization, magnetization saturation and perpendicular magnetic anisotropy field, respectively,  $\Delta H$  is the linewidth and  $H_{\text{f}} = 2\pi f / (\gamma \mu_0)$ .

## References

1. Stamps, R. L. *et al.* The 2014 magnetism roadmap. *J. Phys. D: Appl. Phys.* **47**, 333001 (2014).
2. Ikeda, S. *et al.* A perpendicular-anisotropy CoFeB-MgO magnetic tunnel junction. *Nat. Mater.* **9**, 721 (2010).
3. Fang, B. *et al.* Giant spin-torque diode sensitivity in the absence of bias magnetic field. *Nat. Commun.* **7**, 11259 (2016).
4. Yakata, S. *et al.* Influence of perpendicular magnetic anisotropy on spin-transfer switching current in CoFeB/MgO/CoFeB magnetic tunnel junctions. *J. Appl. Phys.* **105**, 07D131 (2009).
5. Koziol-Rachwał, A. *et al.* Room-temperature perpendicular magnetic anisotropy of MgO/Fe/MgO ultrathin films. *J. Appl. Phys.* **114**, 224307 (2013).
6. Tezuka, N. *et al.* Perpendicular Magnetic Tunnel Junctions With Low Resistance-Area Product: High Output Voltage and Bias Dependence of Magnetoresistance. *IEEE Magn. Lett.* **7**, 1 (2016).
7. Yakushiji, K., Kubota, H., Fukushima, A. & Yuasa, S. Perpendicular magnetic tunnel junction with enhanced anisotropy obtained by utilizing an Ir/Co interface. *Appl. Phys. Express* **9**, 013003 (2016).
8. Yakushiji, K., Fukushima, A., Kubota, H., Konoto, M. & Yuasa, S. Ultralow-voltage spin-transfer switching in perpendicularly magnetized magnetic tunnel junctions with synthetic antiferromagnetic reference layer. *Appl. Phys. Express* **6**, 113006 (2013).
9. Sato, H. *et al.* Properties of magnetic tunnel junctions with a MgO/CoFeB/ta/CoFeB/MgO recording structure down to junction diameter of 11 nm. *Appl. Phys. Lett.* **105**, 062403 (2014).
10. Kugler, Z. *et al.* Co/Pt multilayer-based magnetic tunnel junctions with perpendicular magnetic anisotropy. *J. Appl. Phys.* **111**, 07C703 (2012).
11. Worledge, D. C. *et al.* Spin torque switching of perpendicular Ta/CoFeB/MgO-based magnetic tunnel junctions. *Appl. Phys. Lett.* **98**, 022501 (2011).
12. Oh, S.-C. *et al.* Bias-voltage dependence of perpendicular spin-transfer torque in asymmetric MgO-based magnetic tunnel junctions. *Nat. Phys.* **5**, 898 (2009).
13. Bernert, K. *et al.* Phase diagrams of MgO magnetic tunnel junctions including the perpendicular spin-transfer torque in different geometries. *Phys. Rev. B* **89**, 134415 (2014).
14. Kanak, J. *et al.* Influence of buffer layers on the texture and magnetic properties of co/pt multilayers with perpendicular anisotropy. *Phys. Stat. Sol. A* **204**, 3950 (2007).
15. Zhu, J. *et al.* Voltage-induced ferromagnetic resonance in magnetic tunnel junctions. *Phys. Rev. Lett.* **108**, 197203 (2012).

16. Shiota, Y. *et al.* Induction of coherent magnetization switching in a few atomic layers of FeCo using voltage pulses. *Nat. Mater.* **11**, 39 (2012).
17. Timopheev, A. A., Sousa, R., Chshiev, M., Buda-Prejbeanu, L. D. & Dieny, B. Respective influence of in-plane and out-of-plane spin-transfer torques in magnetization switching of perpendicular magnetic tunnel junctions. *Phys. Rev. B* **92**, 104430 (2015).
18. Sankey, J. C. *et al.* Measurement of the spin-transfer-torque vector in magnetic tunnel junctions. *Nat. Phys.* **4**, 67 (2007).
19. Kubota, H. *et al.* Quantitative measurement of voltage dependence of spin-transfer torque in MgO-based magnetic tunnel junctions. *Nat. Phys.* **4**, 37 (2007).
20. Skowroński, W. *et al.* Influence of MgO tunnel barrier thickness on spin-transfer ferromagnetic resonance and torque in magnetic tunnel junctions. *Phys. Rev. B* **87**, 094419 (2013).
21. Skowroński, W. *et al.* Underlayer material influence on electric-field controlled perpendicular magnetic anisotropy in CoFeB/MgO magnetic tunnel junctions. *Phys. Rev. B* **91**, 184410 (2015).
22. Alzate, J. G. *et al.* Temperature dependence of the voltage-controlled perpendicular anisotropy in nanoscale MgO|CoFeB|Ta magnetic tunnel junctions. *Appl. Phys. Lett.* **104**, 112410 (2014).
23. Nozaki, T. *et al.* Large voltage-induced changes in the perpendicular magnetic anisotropy of an MgO-based tunnel junction with an ultrathin Fe layer. *Phys. Rev. Appl.* **5**, 044006 (2016).
24. Frankowski, M., Chęciński, J., Skowroński, W. & Stobiecki, T. Perpendicular magnetic anisotropy influence on voltage-driven spin-diode effect in magnetic tunnel junctions: A micromagnetic study. *J. Magn. Magn. Mater.* **429**, 11 (2017).
25. Worledge, D. C. & Trouilloud, P. L. Magnetoresistance measurement of unpatterned magnetic tunnel junction wafers by current-in-plane tunneling. *Appl. Phys. Lett.* **83**, 84 (2003).
26. Silva, T. J., Lee, C. S., Crawford, T. M. & Rogers, C. T. Inductive measurement of ultrafast magnetization dynamics in thin-film permalloy. *J. Appl. Phys.* **85**, 7849 (1999).
27. Shiota, Y. *et al.* Quantitative evaluation of voltage-induced magnetic anisotropy change by magnetoresistance measurement. *Appl. Phys. Express* **4**, 043005 (2011).
28. Skowroński, W. *et al.* Magnetic field sensor with voltage-tunable sensing properties. *Appl. Phys. Lett.* **101**, 192401 (2012).
29. Raquet, B. *et al.* Dynamical properties of magnetization reversal in an ultrathin AuCo film. *J. Magn. Magn. Mater.* **150**, L5 (1995).
30. Devolder, T., Le Goff, A. & Nikitin, V. Size dependence of nanosecond-scale spin-torque switching in perpendicularly magnetized tunnel junctions. *Phys. Rev. B* **93**, 224432 (2016).
31. Nembach, H. T. *et al.* Perpendicular ferromagnetic resonance measurements of damping and Landé g-factor in sputtered  $(\text{Co}_2\text{Mn})_{1-x}$  Gex thin films. *Phys. Rev. B* **84**, 054424 (2011).

## Acknowledgements

The authors would like to express their gratitude to Prof. T. Stobiecki for a fruitful discussion and his critical remarks. The project is supported by Polish National Center for Research and Development grant No. LIDER/467/L-6/14/NCBR/2015. Nanofabrication process was performed at Academic Center for Materials and Nanotechnology of AGH University. J.Ch. acknowledges the scholarship under Marian Smoluchowski Krakow Research Consortium KNOW programme. Numerical calculations were supported by PL-GRID infrastructure.

## Author Contributions

J.W. designed sample stack, performed sample deposition and carried out VSM and CIPT measurements, S.Z. and W.S. performed FMR measurements and carried out nanostructurization process, P.R., S.Z. and W.S. performed transport measurements, M.C. created the stability diagram model and performed fitting with an input from W.S., J.Ch. analyzed FMR data and calculated STT and VCMA parameters together with M.F. W.S. wrote the manuscript and supervised the project. All authors reviewed the manuscript.

## Additional Information

**Competing Interests:** The authors declare that they have no competing interests.

**Publisher's note:** Springer Nature remains neutral with regard to jurisdictional claims in published maps and institutional affiliations.



**Open Access** This article is licensed under a Creative Commons Attribution 4.0 International License, which permits use, sharing, adaptation, distribution and reproduction in any medium or format, as long as you give appropriate credit to the original author(s) and the source, provide a link to the Creative Commons license, and indicate if changes were made. The images or other third party material in this article are included in the article's Creative Commons license, unless indicated otherwise in a credit line to the material. If material is not included in the article's Creative Commons license and your intended use is not permitted by statutory regulation or exceeds the permitted use, you will need to obtain permission directly from the copyright holder. To view a copy of this license, visit <http://creativecommons.org/licenses/by/4.0/>.

© The Author(s) 2017